Deterministic control of ferroelastic switching in multiferroic materials

N. Balke[1]*, S. Choudhury[2], S. Jesse[1], M. Huijben[3,4], Y. H. Chu[3,5], A. P. Baddorf[1], L. Q. Chen[2], R. Ramesh[3] and S. V. Kalinin[1,6]

Multiferroic materials showing coupled electric, magnetic and elastic orderings provide a platform to explore complexity and new paradigms for memory and logic devices. Until now, the deterministic control of non-ferroelectric order parameters in multiferroics has been elusive. Here, we demonstrate deterministic ferroelastic switching in rhombohedral $BiFeO_3$ by domain nucleation with a scanning probe. We are able to select among final states that have the same electrostatic energy, but differ dramatically in elastic or magnetic order, by applying voltage to the probe while it is in lateral motion. We also demonstrate the controlled creation of a ferrotoroidal order parameter. The ability to control local elastic, magnetic and torroidal order parameters with an electric field will make it possible to probe local strain and magnetic ordering, and engineer various magnetoelectric, domain-wall-based and strain-coupled devices.

Understanding and controlling polarization switching mechanisms in ferroelectric and multiferroic materials is a critical step towards the realization of oxide-based electronic devices including non-volatile random access memories[1], data storage devices[2], tunnelling barriers[3] and field-effect transistors[4,5]. To date, the above-mentioned applications have invariably been based on 180° ferroelectric polarization switching. The external electric field enables the orientation of the polarization vector to be reversed while maintaining the same spatial axis. Recent progress in scanning probe microscopy (SPM) has allowed the creation of domains as small as 2 nm (ref. 6), demonstrating the feasibility of polarization manipulation on length scales within an order of magnitude of the unit cell size. Complementary to device applications, local control of ferroelectric switching has allowed the role of single defects on domain nucleation[7] and domain wall pinning[8] mechanisms to be examined. However, 180° ferroelectric switching does not alter the magnetization and strain states of the material (as recently confirmed by phase-field simulation)[9], precluding understanding of local behaviour and the control of magnetic and strain order parameters.

Recently, much interest has been directed towards applications of rhombohedral ferroelectrics and multiferroic materials and heterostructures[10]. In heterostructures, non-180° switching opens up an effective pathway for strain-mediated multiferroic coupling[11] and strain-induced metal–insulator transitions in the second material component[12]. In materials such as $BiFeO_3$ (BFO) enhanced conduction at 180° and 109° domain walls has been reported, raising the possibility of applications in novel electronic and memory devices[13]. Finally, given that magnetic ordering in BFO is ferromagnetic in (111) planes and antiferromagnetic between the planes[14], control of non-180° switching is crucial for the development of exchange-coupled magnetoelectric devices[8,10,15–19]. In BFO and similar materials, prime examples of room-temperature multiferroic materials with proper ferroelectricity, the route to controlling magnetic and strain behaviour lies in non-180° polarization switching.

However, symmetry considerations forbid direct manipulation of the non-ferroelectric order parameter using an electric field[20].

This fundamental limitation is belied by the number of phenomenological observations of non-180° switching in BFO. Cruz and colleagues have explored domain switching in BFO using a biased SPM tip and have shown that for BFO grown on (110) $SrTiO_3$ (STO) substrates, 180° walls are formed at lower voltages and 109° domain walls at higher voltages[21]. They were able to improve the stability of otherwise unstable 109° domains after switching by a stack of 180° domain walls between 71° and 109° domain walls (domain wall architecture). Zavaliche and colleagues have demonstrated that both ferroelectric and ferroelastic switching are possible during area poling of BFO grown on (001) STO; however, no further control of the switching process has been reported[22]. The control of in-plane (IP) domain switching on (001)-oriented BFO was achieved by Shafer and colleagues only by using an IP electrode structure[23]. Overall, the SPM single point, SPM area poling, capacitor-based and IP electrode-based switching experiments, as well as phase-field modelling, suggest that ferroelastic polarization switching can proceed along many competing pathways in a seemingly uncontrollable fashion[9,24].

From the theoretical viewpoint, polarization switching in rhombohedral materials is a problem of selection between thermodynamically equivalent pathways. In a prototypical rhombohedral ferroelectric, the polarization vector lies in one of eight equivalent [111] directions. Possible domain orientations for the (001) surface of rhombohedral[25] BFO are shown in Fig. 1a. Application of an electric field in the [001] direction can induce 180° ferroelectric switching, ferroelastic 109° switching in two equivalent states and 71° switching. The equivalence of electrostatic energy gains suggests that the process will be controlled by factors such as the induced strain for non-180° switching, induced electrical energy or defects. Shown schematically in Fig. 1b is an example of a favoured 180° switching represented by the lowest free energy. Note that in the absence of kinetic effects, neither the uniform

[1]The Center for Nanophase Materials Sciences, Oak Ridge National Laboratory, Oak Ridge, Tennessee 37831, USA, [2]Department of Materials Science and Engineering, Pennsylvania State University, University Park, Pennsylvania 16802, USA, [3]Department of Materials Science and Engineering and Department of Physics, University of California, Berkeley, California 94720, USA, [4]Faculty of Science and Technology, MESA+ Institute for Nanotechnology, University of Twente, PO Box 217, 7500 AE, Enschede, The Netherlands, [5]Department of Materials Science and Engineering, National Chiao Tung University, Hsinchu 30010, Taiwan, [6]Materials Sciences and Technology Division, Oak Ridge National Laboratory, Oak Ridge, Tennessee 37831, USA. *e-mail: balken@ornl.gov
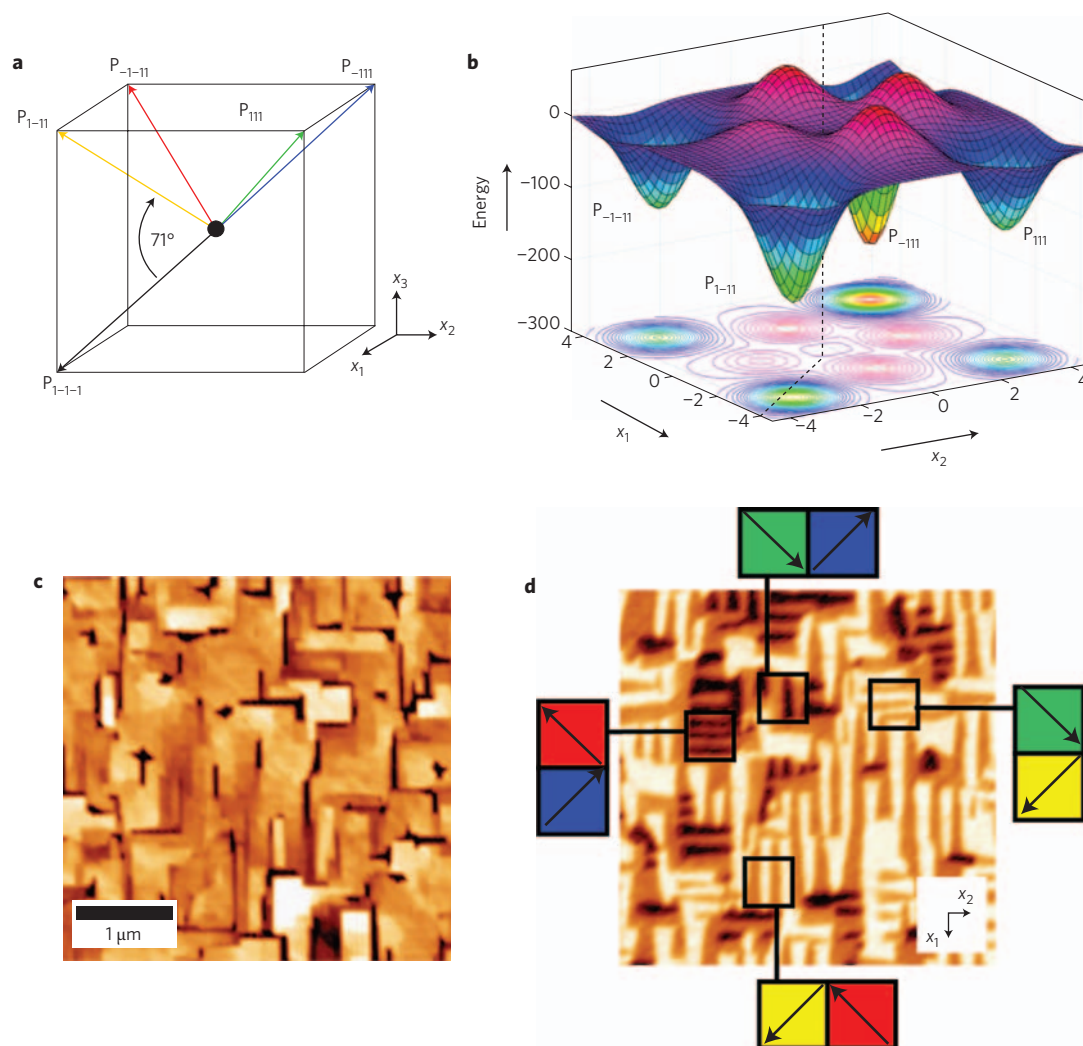
Figure 1 | Ferroelectric domains in BFO. a, Possible directions of the polarization vector P_{x1x2x3} and switching paths in a (001)-oriented rhombohedral ferroelectric. From a given down polarization state, four switching directions are possible when the polarization component is switched into an up polarization state. The 71° polarization switching is shown as an example. To enhance visibility, the crystallographic structure is greatly simplified and only the central Fe ion is shown (black circle). **b**, Schematic of the switching pathways, illustrating different activation and free energies of the final domain states for different switching pathways. **c,d**, Surface topography (**c**) and in-plane PFM image (**d**) of the domain structure of the as-grown BFO/$La_{0.7}Sr_{0.3}MnO_3$ (BFO/LSMO) heterostructures. The domain orientation in the x_1–x_2 plane can be extracted from the PFM contrast and orientation of the striped domains. The domain orientation is indicated for four different areas with the same colour code as used in Fig. 1a. The out-of-plane PFM image shows no contrast and is not shown here.

field in planar capacitors nor the rotationally invariant tip field in an SPM experiment can effectively break the IP symmetry of the material.

In this Article, we demonstrate that selection of the polarization switching pathway is determined by the domain nucleation process. Analysis of the switching mechanisms on the free surface and in the presence of ferroelastic domain walls suggests that the symmetry between possible switching pathways in the rotationally invariant SPM tip field can be broken by lateral tip motion, enabling electric-field manipulation of strain and magnetic order parameters. This approach is used to fabricate predefined ferroelectric domain patterns, including long sought closure domains, as a basis for the creation of toroidal vortex states and other exotic topological defect states.

Determining switching mechanisms

As a model system, we use multiferroic BFO grown on a ferromagnetic $La_{0.7}Sr_{0.3}MnO_3$ electrode on a (001)-oriented STO substrate[15], offering maximal degeneracy between the equivalent polarization

states (see Supplementary Information). Surface topography and IP piezoresponse force microscopy (PFM) images showing the typical stripe ferroelectric domain pattern are shown in Fig. 1c,d[22]. The out-of-plane (OP) PFM image exhibits no contrast due to a preferred downward OP orientation and is not shown here. The as-grown domain walls are mainly uncharged 71° walls[26] and can be determined by the IP PFM images[22,27], as shown in Fig. 1d.

To explore the coupling between IP and OP polarization switching mechanisms, we performed switching spectroscopy PFM (SS-PFM) experiments on pre-existing ferroelastic 71° domain walls. Here, hysteresis loops are acquired on a densely spaced grid of points (50 × 50 points, 10-nm lateral spacing)[28]. The voltage during hysteresis measurement was switched from negative to positive (forward branch) and then from positive to negative (reversed branch). This loading history was chosen to switch the OP polarization component back to its as-grown direction on each point after the hysteresis measurement. Figure 2a shows typical OP hysteresis loops measured on and off the domain walls. Note that the reverse branch of hysteresis loops is virtually independent of
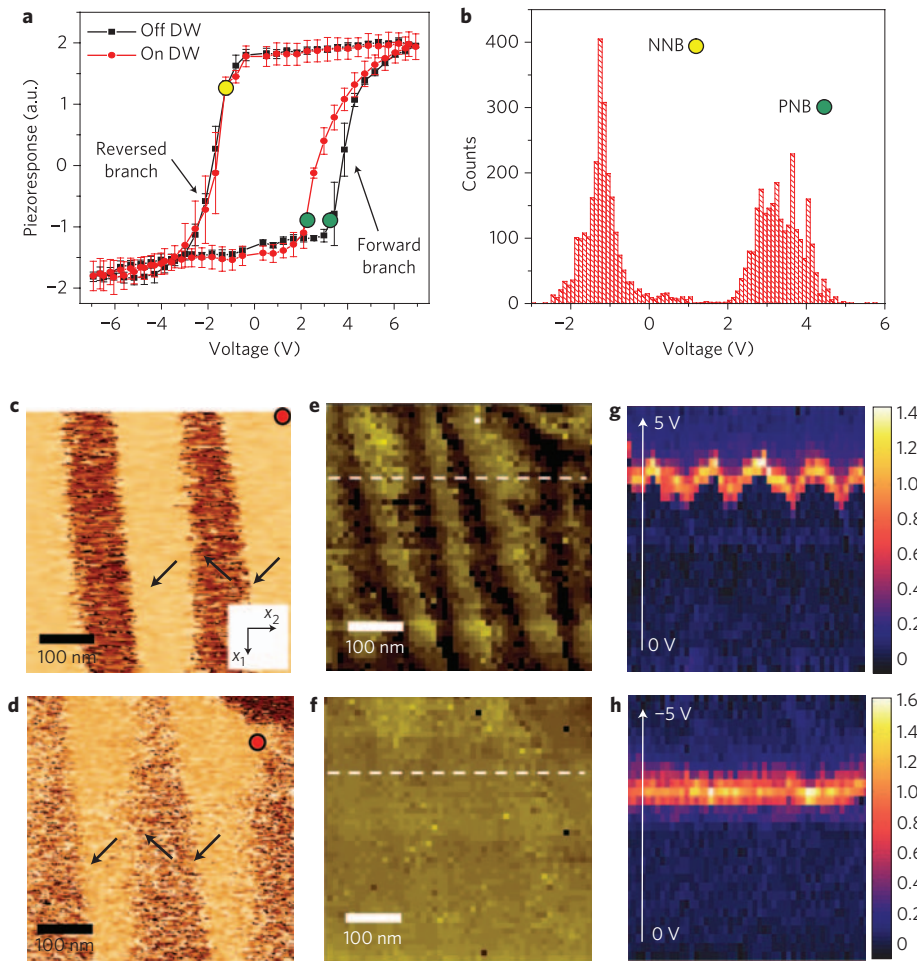
Figure 2 | Switching spectroscopy piezoresponse force microscopy. a, Averaged hysteresis loops in the domain and at the domain wall (DW). Error bars represent the distribution of response at the selected voltage for 10 spatial points, and provide a measure of the uniformity of the switching behaviour. **b**, Histogram of the positive (PNB) and negative nucleation bias (NNB) resulting from the SS-PFM map. **c,d**, In-plane PFM images before (**c**) and after (**d**) mapping. The images differ slightly due to drift (indicated by the red dot) and tip change during mapping. **e,f**, PNB (**e**) and NNB (**f**) maps for the region in Fig. 2d. Note that ferroelastic 71° domain walls strongly affect the PNB, but do not influence the NNB. The data scale is the same as the distribution width in Fig. 2b for PNB and NNB. (Dashed lines are included for use in relation to Fig. 3d.) **g,h**, The spectroscopic dPR/dV–x maps along the selected lines in Fig. 2e,f. The variation of nucleation bias (maximum) across the walls is clearly seen.

position, as is clear from the small error bars on the hysteresis loops. Also, the forward branch in the domain wall and domain centre regions differs greatly, suggesting that the onset of switching for positive fields is greatly reduced at the domain walls. Remarkably, this ferroelectric dynamic is locally reversible, as is clear from a comparison of the IP domain structure before and after the SS-PFM experiment (a small drift of the scanned area is indicated with a red dot; Fig. 2c,d). The onset of switching is characterized by the nucleation bias, defined as the voltage at which the piezoresponse is changed by 3% compared to the saturated state, and is indicated by yellow and green dots in Fig. 2a. The spatial maps of positive (PNB) and negative (NNB) nucleation biases (Fig. 2e,f), corresponding profiles (Fig. 2 g,h) and histograms (Fig. 2b) are presented. A comparison of Fig. 2e and d renders obvious the correlation between nucleation bias for OP polarization switching and ferroelastic 71° domain walls obvious.

These observations suggest that OP polarization switching in (001) rhombohedral ferroelectrics is strongly affected by the presence of an IP ferroelastic domain wall, suggesting a non-trivial coupling between the dynamics of OP and IP polarization components. In the following, we explore the origins of the coupling effect using full three-dimensional modelling of the switching

process and explore whether the coupling can be used to control the IP component.

Modelling polarization dynamics

Switching under the PFM tip was modelled using phase-field modelling. The evolution of the three-dimensional polarization field (P_1, P_2, P_3) is described by the time-dependent Ginzburg-Landau (TDGL) equations

$$\frac{\partial P_i(\mathbf{x}, t)}{\partial t} = -L\frac{\delta F}{\delta P_i(\mathbf{x}, t)}, \quad i = 1, 2, 3$$

where L is a kinetic coefficient related to the domain wall mobility and F the total free energy of the system including bulk, domain wall, elastic energy and electrostatic contributions. The tip-induced potential distribution is approximated by the Lorentz function, $\phi_1(x, y) = \phi_0 c^2/(r^2 + c^2)$, where r is the distance from the tip–surface junction and c the characteristic extent of the electric field of the tip. The latter can be estimated from the observed domain wall width (tip calibration) as $c \approx 10$–30 nm (ref. 29).

The evolution of domain structure on a free surface during tip-induced switching is illustrated in Fig. 3a. Below the nucleation
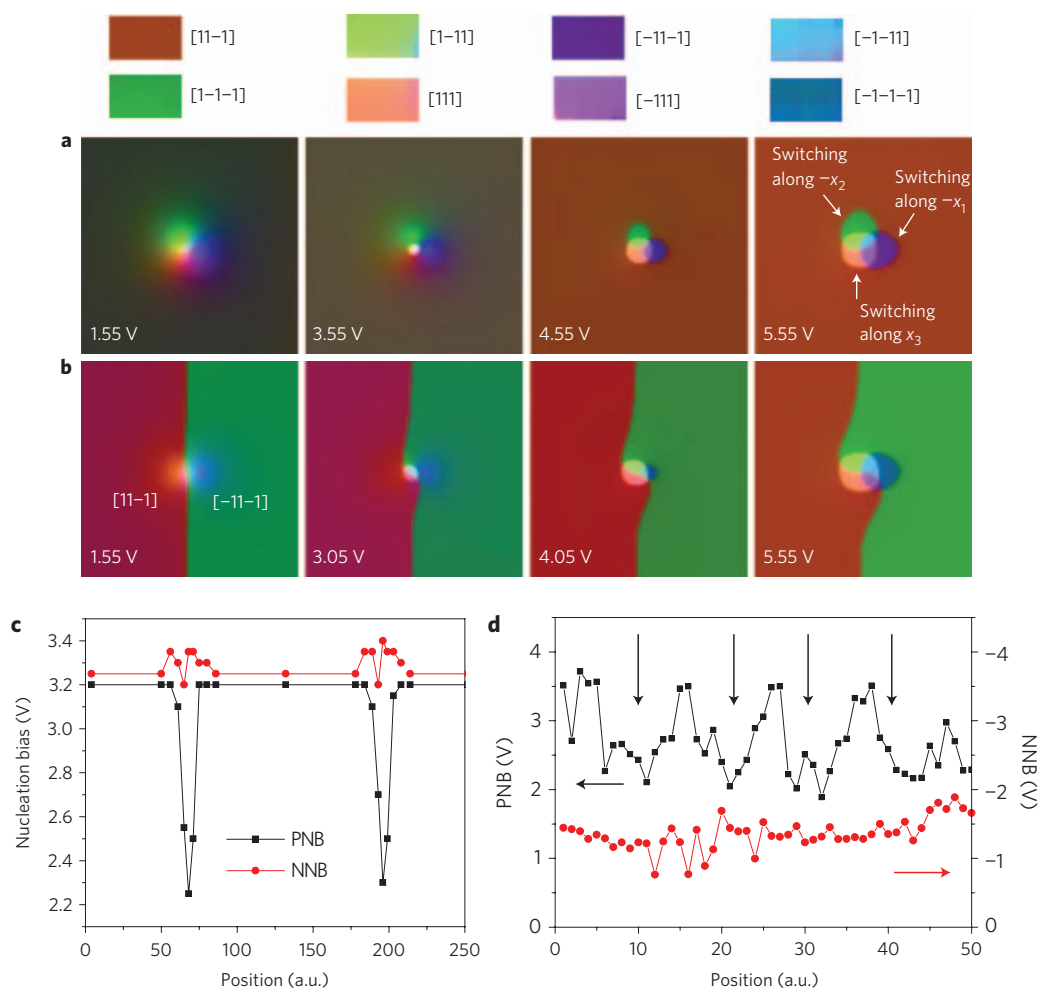
Figure 3 | Phase-field simulations of ferroelectric switching in BFO. a,b, Phase-field simulations of domain nucleation during hysteresis measurements in the domain (**a**) and at a ferroelastic 71° domain wall in BFO (**b**) when different voltages are applied to the piezoresponse force microscopy tip. **c,** Nucleation voltages extracted from the simulations with two 71° domain walls located at position 68 and 196. **d,** Comparison of the simulation and experimental data. The nucleation voltages along the dashed lines in Fig. 2e,f are shown. The black arrows indicate the position of the 71° domain walls.

bias, the tip-induced field perturbs the polarization in the material due to ferroelectric nonlinearity, resulting in an almost rotationally invariant subcritical domain (see Supplementary Information). At the nucleation bias, the normal component of polarization switches (switching along the x_3-direction from [11–1] to [111] is a 71° switching), resulting in the formation of a needle-like domain oriented in the [001] direction. The depolarization field results in rapid elongation of the domain and pinning on the bottom electrode, similar to switching in tetragonal ferroelectrics[30]. Remarkably, the dominant switching mechanism for low voltages is 71°, rather than 180°, despite the larger strain energy of the ferroelastic wall. On increasing the bias, the IP components of the electrostatic field produced by the tip result in switching of the IP polarization components, giving rise to a complex flower-like polarization pattern formed by 71°, 109° and 180° domains. See the Supplementary Information for detailed images of the development of the single polarization components with voltage as top and side views.

This behaviour can be simply explained by the consideration of a depolarization field distribution in the system. Switching of a single polarization component creates a depolarization field in the direction of the switched component that is minimized by the elongation of a needle-like domain, a classical scenario for domain growth[31]. As illustrated by the phase-field modelling, simultaneous switching of two or three polarization components creates a depolarization field acting in the orthogonal directions, favouring half-disc-like

(109° switching) or hemispherical (180° switching) nuclei with correspondingly higher energies. The subsequent evolution of the system depends on the final voltage. Low voltages create a needle-like 71° domain that rapidly spans the film thickness, and near surface 109° and 180° domains that rapidly relax in the zero-field state. For higher voltages, the 180° domain extends through the film and the thermodynamics favours the more stable 180° state, as proposed by Cruz and colleagues[21]. In the following, we demonstrate that the degeneracy between the possible IP domains can be broken by tip motion, allowing for the design of ferroelastic domain patterns.

The switching process at the pre-existing 71° wall is illustrated in Fig. 3b. In this case, even at low voltages the domain wall twists in response to the IP component of the tip field. The onset of twisting is limited only by the activation energy for kink nucleation (two-dimensional Miller–Weinreich nucleus[32]), and is well below the nucleation bias for IP domains. The twist reduces the energy of the 71° nucleus, reducing the nucleation bias. The simulated trend in Fig. 3c matches qualitatively the experimental observation shown in Fig. 3d. On the reverse branch of the hysteresis loop, the domain wall is oriented at 90° to the original orientation, and cannot effectively lower the nucleus energy because the driving force for bending the wall is zero in this case.

A comparison between the phase-field modelling and SS-PFM experiments illustrates that there is a strong coupling between the
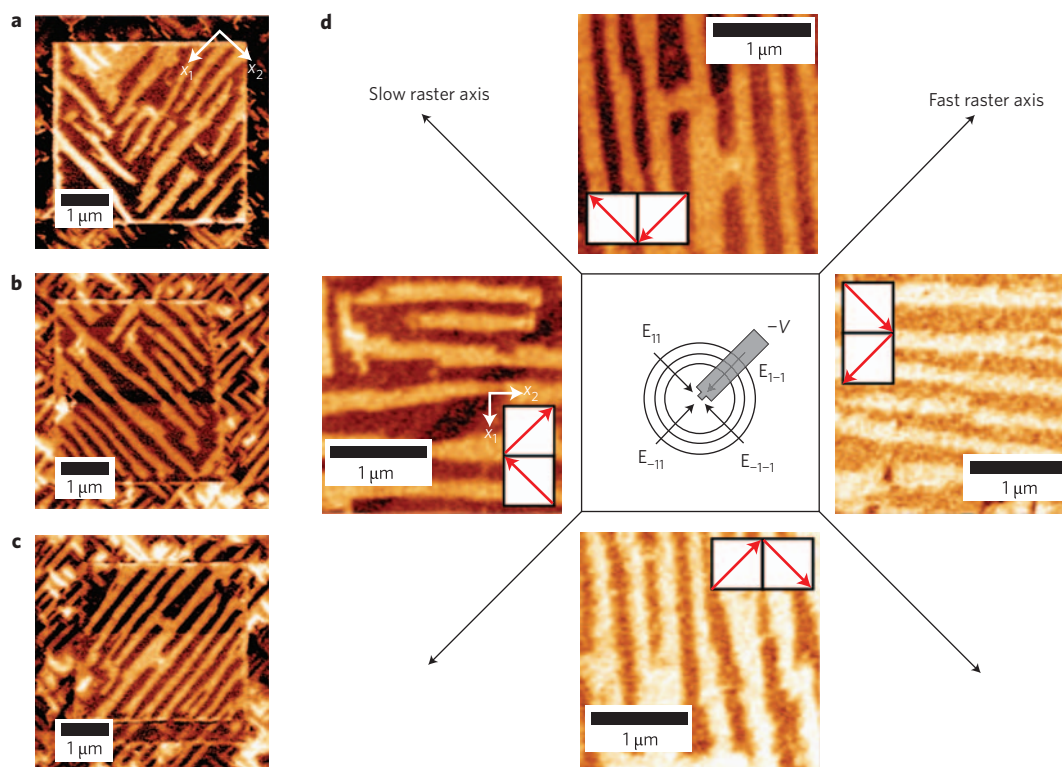
Figure 4 | Tip control of polarization switching mechanisms. a–c, In-plane PFM images of BFO/SrRuO$_3$ heterostructures after standard poling (**a**) and with a decoupled fast raster direction (**b,c**). **d**, Correlation between the direction of fast and slow raster axis during poling and domain orientation after poling. The IP domain orientations are indicated. The inset in the middle shows the tip orientation and the IP electric fields E_{x1x2} acting in the x_1-x_2 plane around a tip biased with negative voltage V. The two domains in each pattern form along the slow raster direction and opposite to the fast raster direction.

dynamics of the OP polarization component and discontinuities in the IP polarization component and that the polarization dynamics are strongly affected by kinetics. In the following, we illustrate that the interplay between these factors can be used to manipulate the IP polarization component.

## Deterministic control of polarization switching

The complex polarization switching mechanisms illustrated in Fig. 3 suggest that the switching between dissimilar IP states is very sensitive to the presence of symmetry-breaking defects. In this section, we demonstrate that the symmetry can be broken artificially, enabling the control of non-180° switching. The basic concept is illustrated in Fig. 4. Application of sufficiently high bias to an SPM tip results in a rotationally invariant field and formation of a complex nucleus containing 71°, 109° and 180° domain regions as shown in the phase-field modelling. The size of each domain is determined by the tip bias, while the lifetime is determined by the size and efficiency of pinning by the lattice, defects and bottom interface. Note that the symmetry between orientations can be effectively broken by moving the tip in the selected direction along the surface, in which case only certain domains are stabilized.

Here, we demonstrate deterministic selection between four possible variants of the stripe patterns in BFO/SrRuO$_3$ (SRO) heterostructures. The stable domain structure in these samples corresponds to stripe domain patterns formed by uncharged 71° domain walls oriented in [11] or [–11] directions along the sample surface in the x_1-x_2 plane. The normal polarization component can be positive or negative, giving rise to eight possible stable domain patterns. During standard area poling, the bias is applied to the scanning tip continuously, and the resulting domain structure shows multiple possible domain variants, as can be seen from the differently oriented stripe domains in Fig. 4a. The OP polarization component is switched

simultaneously during poling (not shown). To control the IP switching process, bias is applied only during trace or retrace motion along the fast raster axis, while otherwise keeping the tip at zero bias. This produces well-ordered domain patterns as shown in Fig. 4b and c, respectively. More details about the time-dependent voltage and the correlation with tip motion are shown in the Supplementary Information.

The combination of bias and motion breaks the rotationally invariant symmetry of the material and tip field and allows control of predefined thermodynamically stable ferroelastic domain patterns. Examples of four possible domain states with an outward OP polarization component written during a single scan are shown in Fig. 4d. For example, motion along the positive slow and fast raster axis (top quadrant in Fig. 4d) results in a domain pattern that consists of domains aligned along the slow and opposite to the fast raster direction. The motion of the biased tip in the positive slow raster direction leaves the [–1–1] domain formed in the wake of the tip motion, while the [11] domain on the front end formed by the E_{11} IP field is constantly deleted. In comparison, tip motion in the positive fast raster direction will result in a [1–1] domain. In this case the domain is formed by $E_{1–1}$ and will not be overwritten by $E_{–11}$ in the wake of the tip motion. If the OP polarization component is switched in the opposite direction by applying a positive instead of a negative voltage to the tip, the directions of the IP fields around the biased tip are reversed and the resulting domain structure is different but can be predicted following the same arguments.

This approach enables the deterministic control of ferroelastic domain switching in rhombohedral ferroelectrics. By this method, artificially designed domain patterns can be created on the macroscopic scale. In Fig. 5, two domain patterns with star and diamond shapes are presented. The differently oriented stripe-like domains are also accompanied by a change of the magnetic
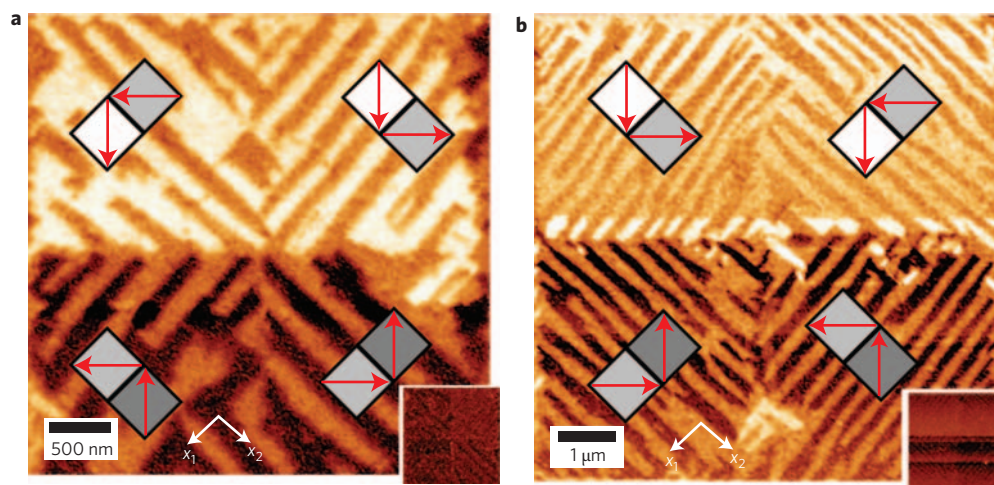
Figure 5 | Engineering domain patterns. a,b, Domain control used to create different macroscopic patterns. Shown are in-plane PFM images of an artificial star (**a**) and diamond domain pattern (**b**) switched with the PFM tip. The insets show the corresponding out-of-plane PFM images and the domain orientations in the x_1-x_2 plane as indicated.
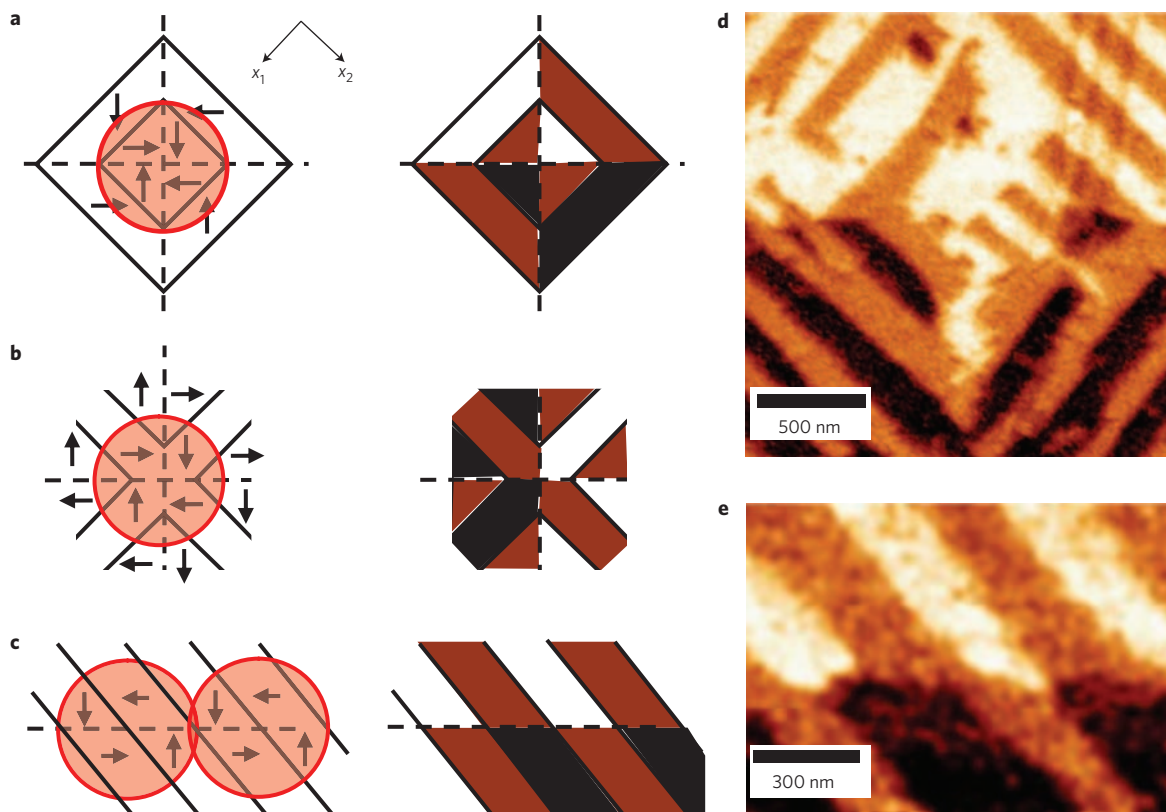
Figure 6 | Creation of closure in-plane domains in BFO. a,b, Possible theoretical domain configurations and corresponding in-plane PFM schemes for BFO/SrRuO$_3$ (SRO) heterostructures showing single closure domains indicated by red circles. **c,** Domain configuration and in-plane PFM images for several closure domain states arranged along a line. **d,** In-plane PFM image after switching a single closure domain with the scheme shown in **a**. The single closure domain is not stable and the area in the middle of Fig. 6d shows reconstruction. **e,** In-plane PFM image after switching several closure domains. The arranged closure domains are stable and the PFM image matches the theoretical PFM pattern (compare **c** and **e**).

planes[11], which enables spatial design of magnetic order parameters. as well as enabling the control of strain and magnetization order parameters, this method can be extended to create topological defects in a polarization field on a small scale. Examples of topological defects are polarization sources/sinks or the celebrated vortex state[33] formed by the closure of IP domains.

Several possible routes to the formation of closure domain states while maintaining 71° domain walls are shown in Fig. 6 together with the predicted IP PFM image for the domain patterns. We distinguish between a single closure domain, which is formed in the middle of four segments of different domain patterns (Fig. 6a,b), and a line of closure domain states formed along the boundary

between two different domain patterns (Fig. 6c). Figure 6d illustrates that a single closure is unstable and the core of the domain pattern reconstructs, leaving the outer closure domain pattern intact. At the same time, the closure domains formed along a line are stabilized by the surrounding domain texture, which differs from Fig. 6a,b because the 71° domain walls go through the centre of the closure domains. The IP PFM image in Fig. 6e shows the predicted PFM image from Fig. 6c, illustrating that closure domain states, the prerequisite for real vortex domain states, can be artificially created, thus generating ferrotoroidal order parameters in ferroelectrics.

Conclusion

The symmetry breaking of the rotationally invariant tip field by tip motion enables deterministic control of non-180° switching in rhombohedral ferroelectrics, and hence local control of strain and magnetic order parameters. These results illustrate the deterministic control of ferroelastic domain patterns in rhombohedral materials, and can be extended to other low symmetry systems, enabling magnetoelectric, strain coupled and related devices. Furthermore, multiple switching states in non-volatile memories and tunnelling barriers can now be explored. Ultimately, combined with polarization-controlled electronic functionality, these studies enable reconfigurable electronics based on manipulation of polarization.

More broadly, these results illustrate that mechanisms of phase transitions leading to equivalent final states can be selected by local stimulus. It was traditionally believed that only biological systems could undergo multiple mechanisms with comparable energies, and phase transitions in inorganic materials were limited to those between a few states controlled by the symmetry of the stimulus field and the symmetry group of the material. Here, we demonstrate that deterministic selection mechanisms in single crystals can be understood, and the mechanisms of defects-mediated control can be resolved.

Materials

BFO/LSMO and BFO/SRO heterostructures were fabricated by pulsed-laser deposition with reflection high-energy electron diffraction (RHEED) control of the growth process. Atomically smooth TiO_2-terminated $SrTiO_3$ (STO) (100) substrates were prepared by a combined HF-etching/anneal treatment. All substrates had vicinal angles of ~0.1°. Stoichiometric LSMO, SRO and BFO targets were ablated at a laser fluence of ~1.5 J cm^{-2} and a repetition rate of 1 or 2 Hz for the growth of LSMO/SRO and BFO, respectively. During growth, the substrate was held at 750 °C in an oxygen environment at 200 mtorr for LSMO[34]. For SRO and BFO the conditions were adjusted to 670 °C and 100 mtorr (ref. 35). RHEED analysis demonstrated intensity oscillations indicating a layer-by-layer growth mode without island formation. After growth, the heterostructures were slowly cooled to room temperature in 1 atm of oxygen at a rate of ~5 °C min^{-1} to optimize oxidation.

Experimental setup

SSPFM was implemented on a commercial SPM system (Veeco MultiMode with Nanoscope-IIIA controller) equipped with external data-acquisition electronics based on a NI-6115 fast DAQ card to generate the probing signal, store local hysteresis loops, and correlate them with surface topography. The tip was oriented along the [110] direction in order to control IP domain contrast[26]. SSPFM was performed on a 50×50 grid with a 10-nm grid spacing to characterize the switching of the OP polarization component over a large range[28]. For imaging, an a.c. voltage of 1 V peak-to-peak and a maximum switching voltage of ±7 V were applied during the measurement. For each point, two subsequent cycles were measured and the average loop for each point calculated and analysed. Nucleation was defined as the point in the hysteresis loop where the signal deviates from a constant value by a set-point value of 3%. For the area poling experiments, a tip velocity of 2 μm s^{-1} and poling voltages of –8 V (applied to the tip) were used.

Phase-field modelling

TDGL equations were solved using the semi-implicit Fourier spectral method[36] on a $128\Delta x \times 128\Delta x \times 36\Delta x$ mesh with periodic boundary conditions along the x_1 and x_2 axes, where Δx is the simulation grid spacing. The thickness of the film was taken to be $h_f = 20\Delta x$. The dielectric stiffness used to calculate the bulk energy along with the elastic and the electrostrictive coefficients used in the elastic energy calculation were obtained from ref. 37. The substrate was assumed to exert a biaxial compressive strain of 1%. The gradient energy coefficients were chosen as $G_{11}/G_{110} = 0.4$. The width of the 180° domain wall and the corresponding domain wall energy were taken to be similar in magnitude to those of other perovskite ferroelectric systems[38]. For electrostatic energy calculations, we used $\kappa_{11} = \kappa_{22} = \kappa_{33} = 100$. To find the critical nucleation potential, the potential ϕ_0 was gradually increased with an increment of 0.05 V, and the domain structure from a previous simulation was used as the input at each increment of the potential. The nucleation potential was identified as that corresponding to the discontinuous jump in polarization below the probe as a function of the field.

References

1. Scott, J. *Ferroelectric Memories* (Springer Verlag, 2000).
2. Tybell, T., Ahn, C. H. & Triscone, J. M. Control and imaging of ferroelectric domains over large areas with nanometer resolution in atomically smooth epitaxial $Pb(Zr_{0.2}Ti_{0.8})O_3$ thin films. *Appl. Phys. Lett.* **72,** 1454–1456 (1998).
3. Tsymbal, E. Y. & Kohlstedt H. Applied physics—tunneling across a ferroelectric. *Science* **313,** 181–183 (2006).
4. Miller, S. L. & McWhorter, P. J. Physics of the ferroelectric nonvolatile memory field-effect transistor. *J. Appl. Phys.* **72,** 5999–6010 (1992).
5. Mathews, S., Ramesh, R., Venkatesan, T. & Benedetto, J. Ferroelectric field effect transistor based on epitaxial perovskite heterostructures. *Science* **276,** 238–240 (1997).
6. Tanaka, K. *et al.* Scanning nonlinear dielectric microscopy nano-science and technology for next generation high density ferroelectric data storage. *Jpn J. Appl. Phys.* **47,** 3311–3325 (2008).
7. Jesse, S. *et al.* Direct imaging of the spatial and energy distribution of nucleation centres in ferroelectric materials. *Nature Mater.* **7,** 209–215 (2008).
8. Paruch, P., Giamarchi, T. & Triscone, J. M. Domain wall roughness in epitaxial ferroelectric $PbZr_{0.2}Ti_{0.8}O_3$ thin films. *Phys. Rev. Lett.* **94,** 197601 (2005).
9. Li, L. J., Li, J. Y., Shu, Y. C. & Yen, J. H. The magnetoelectric domains and cross-field switching in multiferroic $BiFeO_3$. *Appl. Phys. Lett.* **93,** 192506 (2008).
10. Ramesh, R. & Spaldin, N. A. Multiferroics: progress and prospects in thin films. *Nature Mater.* **6,** 21–29 (2007).
11. Chu, Y. H. *et al.* Electric-field control of local ferromagnetism using a magnetoelectric multiferroic. *Nature Mater.* **7,** 478–482 (2008).
12. Takamura, Y. *et al.* Tuning magnetic domain structure in nanoscale $La_{0.7}Sr_{0.3}MnO_3$ islands. *Nano Lett.* **6,** 1287–1291 (2006).
13. Seidel, J. *et al.* Conduction at domain walls in oxide multiferroics. *Nature Mater.* **8,** 229–234 (2009).
14. Catalan, G. & Scott, J. F. Physics and applications of bismuth ferrite. *Adv. Mater.* **21,** 2463–2485 (2009).
15. Bea, H. *et al.* Mechanisms of exchange bias with multiferroic $BiFeO_3$ epitaxial thin films. *Phys. Rev. Lett.* **100,** 017204 (2008).
16. Bea, H. *et al.* Tunnel magnetoresistance and robust room temperature exchange bias with multiferroic $BiFeO_3$ epitaxial thin films. *Appl. Phys. Lett.* **89,** 242114 (2006).
17. Dho, J., Qi, X., Kim, H., MacManus-Driscoll, J. L. & Blamire, M. G. Large electric polarization and exchange bias in multiferroic $BiFeO_3$. *Adv. Mater.* **18,** 1445–1448 (2006).
18. Gajek, M. *et al.* Tunnel junctions with multiferroic barriers. *Nature Mater.* **6,** 296–302 (2007).
19. Bea, H. *et al.* Combining half-metals and multiferroics into epitaxial heterostructures for spintronics. *Appl. Phys. Lett.* **88,** 062502 (2006).
20. Hill, N. A. Why are there so few magnetic ferroelectrics? *J. Phys. Chem. B* **104,** 6694–6709 (2000).

21. Cruz, M. P. *et al.* Strain control of domain-wall stability in epitaxial BiFeO$_3$ (110) films. *Phys. Rev. Lett.* **99,** 217601 (2007).
22. Zavaliche, F. *et al.* Polarization switching in epitaxial BiFeO$_3$ films. *Appl. Phys. Lett.* **87,** 252902 (2005).
23. Shafer, P. *et al.* Planar electrode piezoelectric force microscopy to study electric polarization switching in BiFeO$_3$. *Appl. Phys. Lett.* **90,** 202909 (2007).
24. Shu, Y. C., Yen, J. H., Chen, H. Z., Li, J. Y. & Li, L. J. Constrained modeling of domain patterns in rhombohedral ferroelectrics. *Appl. Phys. Lett.* **92,** 052909 (2008).
25. Kubel, F. & Schmid, H. Structure of a ferroelectric and ferroelastic monodomain crystal of the perovskite BiFeO$_3$. *Acta Cryst. B* **46,** 698–702 (1990).
26. Zavaliche, F. *et al.* Multiferroic BiFeO$_3$ films: domain structure and polarization dynamics. *Phase Transitions* **79,** 991–1017 (2006).
27. Zavaliche, F. *et al.* Ferroelectric domain structure in epitaxial BiFeO$_3$ films. *Appl. Phys. Lett.* **87,** 182912 (2005).
28. Jesse, S., Lee, H. N. & Kalinin, S. V. Quantitative mapping of switching behavior in piezoresponse force microscopy. *Rev. Sci. Instr.* **77,** 073702 (2006).
29. Kalinin, S. V. *et al.* Intrinsic single-domain switching in ferroelectric materials on a nearly ideal surface. *Proc. Natl Acad. Sci. USA* **104,** 20204–20209 (2007).
30. Molotskii, M. *et al.* Ferroelectric domain breakdown. *Phys. Rev. Lett.* **90,** 107601 (2003).
31. Landauer, R. Electrostatic considerations in BaTiO$_3$ domain formation during polarization reversal. *J. Appl. Phys.* **28,** 227–234 (1957).
32. Miller, R. & Weinreich, G. Mechanism for the sidewise motion of 180° domain walls in barium titanate. *Phys. Rev.* **117,** 1460–1466 (1960).
33. Naumov, I. I., Bellaiche, L. & Fu, H. Unusual phase transitions in ferroelectric nanodisks and nanorods. *Nature* **432,** 737–740 (2004).
34. Huijben, M. *et al.* Critical thickness and orbital ordering in ultrathin La$_{0.7}$Sr$_{0.3}$MnO$_3$ films. *Phys. Rev. B* **78,** 094413 (2008).
35. Martin, L. W. *et al.* Nanoscale control of exchange bias with BiFeO$_3$ thin films. *Nano Lett.* **8,** 2050–2055 (2008).
36. Chen, L. Q. & Shen, J. Applications of semi-implicit Fourier-spectral method to phase field equations. *Comput. Phys. Commun.* **108,** 147–158 (1998).
37. Zhang, J. X. *et al.* Computer simulation of ferroelectric domain structures in epitaxial BiFeO$_3$ thin films. *J. Appl. Phys.* **103,** 094111 (2008).
38. Chen, Y. B. *et al.* Ferroelectric domain structures of epitaxial (001) BiFeO$_3$ thin films. *Appl. Phys. Lett.* **90,** 072907 (2007).

Acknowledgements

Author contributions

N.B. conceived, designed and conducted the experiments, and wrote the article. S.C. and L.Q.C. performed modelling. M.H., Y.H.C. and R.R. contributed materials and S.J. developed spectroscopic measurement technique and analysis tools. S.V.K. and A.P.B. co-wrote the article. All authors discussed the results and commented on the manuscript.

Additional information

Supplementary information accompanies this paper at www.nature.com/naturenanotechnology. Reprints and permission information is available online at http://npg.nature.com/reprintsandpermissions/. Correspondence and requests for materials should be addressed to N.B.